Available online at www.sciencedirect.com
ScienceDirect
Icarus 193 (2008) 233–251
ICARUS
www.elsevier.com/locate/icarus

Identification of spectral units on Phoebe

A. Coradini [a,*], F. Tosi [a], A.I. Gavrishin [c], F. Capaccioni [b], P. Cerroni [b], G. Filacchione [b], A. Adriani [a], R.H. Brown [d], G. Bellucci [a], V. Formisano [a], E. D'Aversa [a], J.I. Lunine [d,a], K.H. Baines [f], J.-P. Bibring [g], B.J. Buratti [f], R.N. Clark [h], D.P. Cruikshank [i], M. Combes [j], P. Drossart [j], R. Jaumann [k], Y. Langevin [g], D.L. Matson [f], T.B. McCord [l], V. Mennella [m], R.M. Nelson [f], P.D. Nicholson [n], B. Sicardy [j], C. Sotin [o], M.M. Hedman [n], G.B. Hansen [l], C.A. Hibbitts [p], M. Showalter [i], C. Griffith [d], G. Strazzulla [e]

[a] *INAF-IFSI, Istituto di Fisica dello Spazio Interplanetario, Area Ricerca Tor Vergata, Via Fosso del Cavaliere 100, I-00133 Roma, Italy*
[b] *INAF-IASF, Istituto di Astrofisica Spaziale e Fisica Cosmica, Area Ricerca Tor Vergata, Via Fosso del Cavaliere 100, I-00133 Roma, Italy*
[c] *South-Russian State Technical University, Prosveschenia 132, Novocherkassk 346428, Russia*
[d] *Lunar and Planetary Laboratory and Steward Observatory, 1629 University Boulevard, University of Arizona, Tucson, AZ 85721, USA*
[e] *INAF-OACT, Osservatorio Astrofisico di Catania, Via S. Sofia 78, I-95123 Catania, Italy*
[f] *Jet Propulsion Laboratory, 4800 Oak Grove Drive, Pasadena, CA 91109, USA*
[g] *Institut d'Astrophysique Spatiale, Université de Paris-Sud, Bâtiment 121, F-91405 Orsay, France*
[h] *US Geological Survey, Mail Stop 964, Box 25046, Denver Federal Center, Denver, CO 80225, USA*
[i] *NASA Ames Research Center, Moffett Field, CA 94035-1000, USA*
[j] *Observatoire de Paris-Meudon, 5 place Jules Janssen, F-92190 Meudon, France*
[k] *Institute for Planetary Exploration, German Aerospace Center (DLR), Rutherfordstrasse 2, D-12489 Berlin, Germany*
[l] *Department of Earth and Space Sciences, University of Washington, 310 Condon Hall, Box 351310, Seattle, WA 98195-1310, USA*
[m] *INAF-OAC, Osservatorio Astronomico di Capodimonte, Salita Moiariello 16, I-80131 Napoli, Italy*
[n] *Cornell University, 418 Space Sciences Building, Ithaca, NY 14853, USA*
[o] *Laboratoire de Planétologie et Géodynamique, Université de Nantes, 2 rue de la Houssinière, B.P. 92208, F-44322 Nantes Cedex 3, France*
[p] *Planetary Sciences Institute NW, 225 S. Lake Avenue, Suite 300, Pasadena, CA 91101, USA*

Received 26 October 2006; revised 2 July 2007

Available online 15 September 2007

Abstract

We apply a multivariate statistical method to the Phoebe spectra collected by the VIMS experiment onboard the Cassini spacecraft during the flyby of June 2004. The G-mode clustering method, which permits identification of the most important features in a spectrum, is used on a small subset of data, characterized by medium and high spatial resolution, to perform a raw spectral classification of the surface of Phoebe. The combination of statistics and comparative analysis of the different areas using both the VIMS and ISS data is explored in order to highlight possible correlations with the surface geology. In general, the results by Clark et al. [Clark, R.N., Brown, R.H., Jaumann, R., Cruikshank, D.P., Nelson, R.M., Buratti, B.J., McCord, T.B., Lunine, J., Hoefen, T., Curchin, J.M., Hansen, G., Hibbitts, K., Matz, K.-D., Baines, K.H., Bellucci, G., Bibring, J.-P., Capaccioni, F., Cerroni, P., Coradini, A., Formisano, V., Langevin, Y., Matson, D.L., Mennella, V., Nicholson, P.D., Sicardy, B., Sotin, C., 2005. Nature 435, 66–69] are confirmed; but we also identify new signatures not reported before, such as the aliphatic CH stretch at 3.53 μm and the ∼4.4 μm feature possibly related to cyanide compounds. On the basis of the band strengths computed for several absorption features and for the homogeneous spectral types isolated by the G-mode, a strong correlation of CO_2 and aromatic hydrocarbons with exposed water ice, where the uniform layer covering Phoebe has been removed, is established. On the other hand, an anti-correlation of cyanide compounds with CO_2 is suggested at a medium resolution scale.

* Corresponding author. Fax: +39 06 4993 4182.
E-mail address: coradini@ifsi-roma.inaf.it (A. Coradini).

0019-1035/$ – see front matter
doi:10.1016/j.icarus.2007.07.023

Keywords: Saturn, satellites; Satellites, composition; Irregular satellites; Spectroscopy

1. Introduction

Phoebe, ninth satellite of Saturn (S IX), was discovered by W.H. Pickering in 1898. Phoebe has several peculiar properties. Its retrograde orbit, with large semi major axis (12.952 million km or 214.9 Saturn radii, >10 times the one of Titan), coupled with its relatively high eccentricity ($e = 0.1644$) and high inclination ($i = 174.75°$), suggests that this moon had not formed in the Saturn environment, but is an external body permanently trapped by Saturn's gravity (Pollack et al., 1979). From this point of view, Phoebe resembles the outermost satellites of Jupiter, Uranus and Neptune, which are "irregular" as well.

Images taken from the Voyager 2 spacecraft on 4 September 1981, despite the great distance of the flyby (2.076 million km), had first shown that Phoebe is a roughly spherical and dark object with a diameter of about 210 km and a mean albedo of 0.07, with some isolated, quasi-circular bright spots at high northern and southern latitudes, which exhibit albedos up to 0.11, i.e., ∼50% greater than the rest of the dark, bland areas (Thomas et al., 1983). Unfortunately, the low resolution Voyager images did not permit inferring the origin of these bright markings; nonetheless, from these and other spectrophotometric data, Phoebe was initially related to C-type and D-type asteroids, like the "Trojan" asteroids moving on Jupiter's orbit or the "Centaurs" orbiting between Jupiter and Neptune (Cruikshank et al., 1983, 1984). Phoebe's dimensions and its asynchronous rotational period (9.2735 ± 0.0006 h; Bauer et al., 2004) are also similar to those measured for many asteroids. Furthermore, Phoebe was invoked to be the source of the dark material coating the leading hemisphere of Iapetus: according to the first version of the exogenous model (Soter, 1974), particles from Phoebe spiraled towards Saturn in retrograde orbits due to the Poynting–Robertson effect, and collided with Iapetus' leading side.

On 11 June 2004, the real nature of this satellite was uncovered during the flyby of Cassini–Huygens. Some 19 days before the spacecraft entered orbit around Saturn, it reached the closest approach of 2068 km from Phoebe, i.e., ∼1000 times closer than the Voyager 2, at 19:33 SCET (*spacecraft event time* or UTC onboard the spacecraft), with a relative velocity of 6.35 $\mathrm{km\,s^{-1}}$. The average diameter of Phoebe was determined to be about 213 km, whereas its mass was inferred from precise tracking of the spacecraft and optical navigation. The measurements yielded a value of $\mathrm{GM} = 0.5527 \pm 0.001\ \mathrm{km^3\,s^{-2}}$ (Jacobson et al., 2004); this, combined with an accurate volume estimate from the images, led to a calculated mean density of about $1630 \pm 33\ \mathrm{kg\,m^{-3}}$ (Jacobson et al., 2004), much lighter than most rocks, but heavier than pure water ice at approximately $930\ \mathrm{kg\,m^{-3}}$. This value is higher than the mass-averaged density of the regular satellites of Saturn, again supporting the evidence that Phoebe is a captured body (Johnson and Lunine, 2005).

From the images acquired by the Cassini multispectral camera, Phoebe appeared to be an irregularly shaped body, with overlapping craters of varying sizes. This morphology suggests an old surface. The many craters smaller than 1 km indicate that projectiles smaller than 100 m once bombarded Phoebe. All of the images show evidence for an ice-rich body mantled with a layer of dusty dark material, whose thickness can change from area to area (see Fig. 1). Further evidence for this can be seen on some crater walls where the darker material appears to have slid downwards, exposing more light-colored material.

The first spectral analysis performed on the VIMS data (Clark et al., 2005) pointed out the existence of ferrous iron-bearing minerals, bound water, carbon dioxide, probable phyllosilicates, organics and cyanide compounds. This mix of surface materials has not been encountered elsewhere: the emerging view of Phoebe is that it might have been part of an ancestral population of icy, comet-like bodies, some of which now reside in the Kuiper belt beyond Neptune.

The quality of Cassini data enables more detailed analyses on selected areas of the satellite. The application of the G-mode method to the infrared spectra of Phoebe acquired by VIMS—essentially an automatic classification of its surface—allows us to identify some spectral features correlated with location or geology on the satellite; moreover, this is also a test of the reliability of the method, to be used in the future on other VIMS observations of Saturn's icy moons.

2. The VIMS instrument

The *Visual and Infrared Mapping Spectrometer* (VIMS) is an imaging spectrometer onboard the Cassini Orbiter spacecraft. VIMS is actually made up of two spectrometers, VIMS-V (developed in Italy) and VIMS-IR (developed in the USA). VIMS is the result of an international collaboration involving the space agencies of the United States, Italy, France and Germany (Miller et al., 1996) as well as other academic and industrial partners.

The two channels share a common electronics box and are co-aligned on a common optical pallet. The combined optical system generates 352 two-dimensional images (with maximum nominal dimensions of 64×64, 0.5 mrad pixels), each one corresponding to a specific spectral channel. These images are merged by the main electronics in order to produce "image cubes" representing the spectrum of the same field of view (FOV) in the range from 0.35 to 5.1 μm, sampled in 352 bands. See Brown et al. (2004) for a complete description of the instrument (Table 1).

In the following, we considered only the IR portion of VIMS spectra, i.e., the data acquired by VIMS-IR. Infrared data are generally more diagnostic for the composition of solid surfaces; however, in principle, the classification operated by the G-mode can be performed on the basis of all of the available bands, especially when both VIMS-V and VIMS-IR operate in nominal

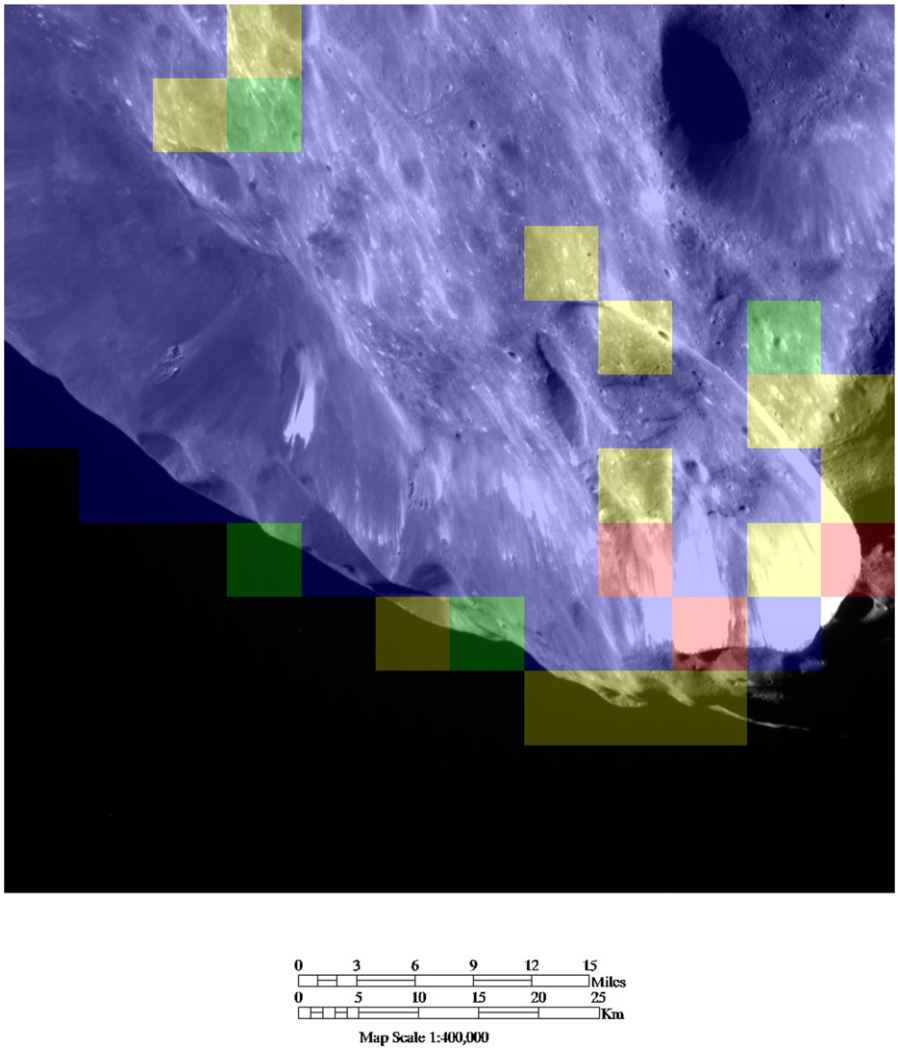

Fig. 1. Combined map of ISS NAC and infrared image taken from VIMS cube "A." The dimensions of the two FOVs are similar (0.34° VIMS, 0.35° ISS). From the inspection of the optical image, it appears that the Phoebe craters are very peculiar, with landslides on the inside walls revealing exposed subsurface material. The color code is related to the average spectra shown in Fig. 3e. The colorless pixels of the target are related to spectra discarded by the processing.

Table 1
VIMS specifications summary

	VIMS-V	VIMS-IR
Spectral coverage (μm)	0.35–1.05	0.85–5.1
Spectral channels (bands)	96	256
Average spectral sampling (nm/channel)	7.3	16.6
Total FOV (°)	1.83 × 1.83	1.83 × 1.83
Total FOV (mrad)	32 × 32	32 × 32
Nominal IFOV (mrad)	0.50 × 0.50	0.50 × 0.50
Hi-res IFOV (mrad)	0.167 × 0.167	0.25 × 0.50
Nominal image dimension (pixel)	1 × 1, 6 × 6, 12 × 12, 64 × 64	1 × 1, 6 × 6, 12 × 12, 64 × 64
Detector type	Si CCD (2D)	InSb photodiodes (1D)
Average SNR	380	100

IFOV mode so that their acquisitions are spatially consistent, even though the consequent use of a very large number of variables with the G-mode method is still to be explored.

To try to correlate various spectral groupings with the surface geology of Phoebe, we have used the Imaging Science System (ISS) data on the Planetary Data System (PDS) database available on the Internet (http://pds.jpl.nasa.gov).

3. The classification method

In this work, a multivariate analysis has been carried out, which is useful in the case of hyperspectral data like those acquired by VIMS, showing a large informative content. Typically a large number of samples (spectra) are averaged in order to increase the signal-to-noise ratio (SNR). In our approach, aver-

Table 2
Summary of the four VIMS cubes used in this work

Cube	PDS filename	Subsequence	Spatial dimensions	Pixels of the target	Integration time per pixel (ms)	Phase angle (degrees)	IFOV mode	Spatial resolution (km/pixel)
A	V1465673135_1	PHOEBE015	12 × 12	101	300	78.1	NOMINAL	6.15 × 6.15
B	V1465677443_1	PHOEBE017	64 × 18	475	160	85.9	HIGH	3.79 × 7.59
C	V1465674369_1	PHOEBE017	12 × 12	144	180	62.8	NOMINAL	2.39 × 2.39
D	V1465674828_1	PHOEBE017	12 × 12	144	180	37.4	NOMINAL	1.24 × 1.24

Table 3
Permanent and temporary artifacts in VIMS-IR data during the Phoebe flyby

VIMS-IR spectral channel	Wavelength (μm)	Artifact
23	1.24660	Hot spectral channel
46–48	1.62040–1.65970	Order-sorting filter
127–129	2.96560–2.99550	Order-sorting filter
143	3.23190	Hot spectral channel
179	3.83580	Hot spectral channel
180–182	3.85310–3.88020	Order-sorting filter
210	4.35130	Hot spectral channel
235	4.77210	Hot spectral channel

ages are made only on subsets of samples that are statistically close each other on the basis of the most meaningful variables. The clustering method we used for the classification is the *G-mode*.

The G-mode method was originally developed by A.I. Gavrishin and A. Coradini (see Gavrishin et al., 1980, 1992; Coradini et al., 1976, 1977) to classify lunar samples on the basis of the major oxides composition. The good results obtained warranted its application to several different data sets (see, for example, Coradini et al., 1976, 1983; Carusi and Massaro, 1978; Bianchi et al., 1980; Gavrishin et al., 1980; Giovannelli et al., 1981; Barucci et al., 1987; Orosei et al., 2003). In particular, the Imaging Spectrometer for Mars (ISM), flown onboard the Soviet Phobos mission, offered the first chance to apply the G-mode method to imaging spectroscopy data (Coradini et al., 1991; Erard et al., 1991; Cerroni and Coradini, 1995).

The G-mode differs from other widely used statistical methods—such as the Principal Components Analysis (PCA) and the *Q*-mode method—in some key characteristics (see Bianchi et al., 1980): in summary, a linear dependence of the variables is not needed; instrumental errors can be taken into account; meaningless variables are discerned and removed; and finally different levels of classification can be performed.

Basically, by lowering the confidence level of the test, set a priori by the user, the algorithm can perform a more refined classification, in order to look for further homogeneous types. In this case, the G-mode includes a test that allows to interrupt the classification when it becomes too detailed: when the statistical distance among types becomes smaller than the established confidence level, the algorithm can either stop or continue by merging different small types together (this condition is reported in the output of the program).

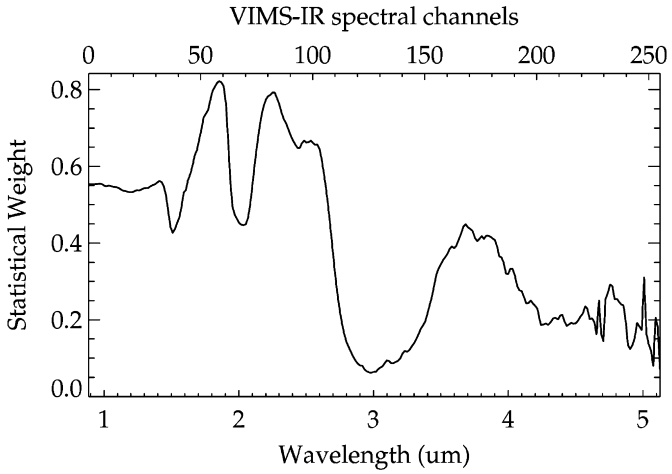

Fig. 2. Statistical weights of the variables in the case of an absolute error of 0.001 and 99.5% confidence level. For a classification obtained with the same error for all the variables, the statistical weights of the variables show a trend similar to Phoebe's infrared spectrum as observed by VIMS. This is expected since, by assuming the same error for all of the variables, the classification is naturally driven by the spectral bands which show the highest reflectance and that are more diagnostic. For instance, in this case, the large water absorption feature cent red at ∼3 μm is scarcely significant for our aim, being always present in all the spectra.

4. The VIMS data set

During the Phoebe flyby, acquisitions by VIMS lasted more than one day. The global dataset is made up of 292 cubes acquired during sequence S01, the first Saturn tour sequence. These acquisitions cover a range of angular resolutions (given by the spacecraft distance and the instrumental field of view or IFOV, namely the angular resolution being used), phase angles and integration times.

The acquisitions run from 11 June 2004, 08:48 SCET, at an initial range of 245,836 km and phase angle of 86.7°, until 12 June, 10:19 SCET, at a final range of about 337,712 km and phase angle of 92.5°. The closest VIMS cube was acquired on 11 June at 19:32 SCET, from 2100 km and with ∼25° phase angle.

The best spatial resolution achieved by VIMS in nominal IFOV mode is ∼1 km/pixel; data showing this kind of resolution are those coded V1465672565-7670, referring to the subsequences PHOEBE015 and PHOEBE017 which were acquired just before and after the closest point approach. For several subsequences, other instruments of the Remote Sensing Pallet (RPS) were working together with VIMS.

In this paper, we show four examples of classification obtained through the G-mode on as many cubes (named, in the

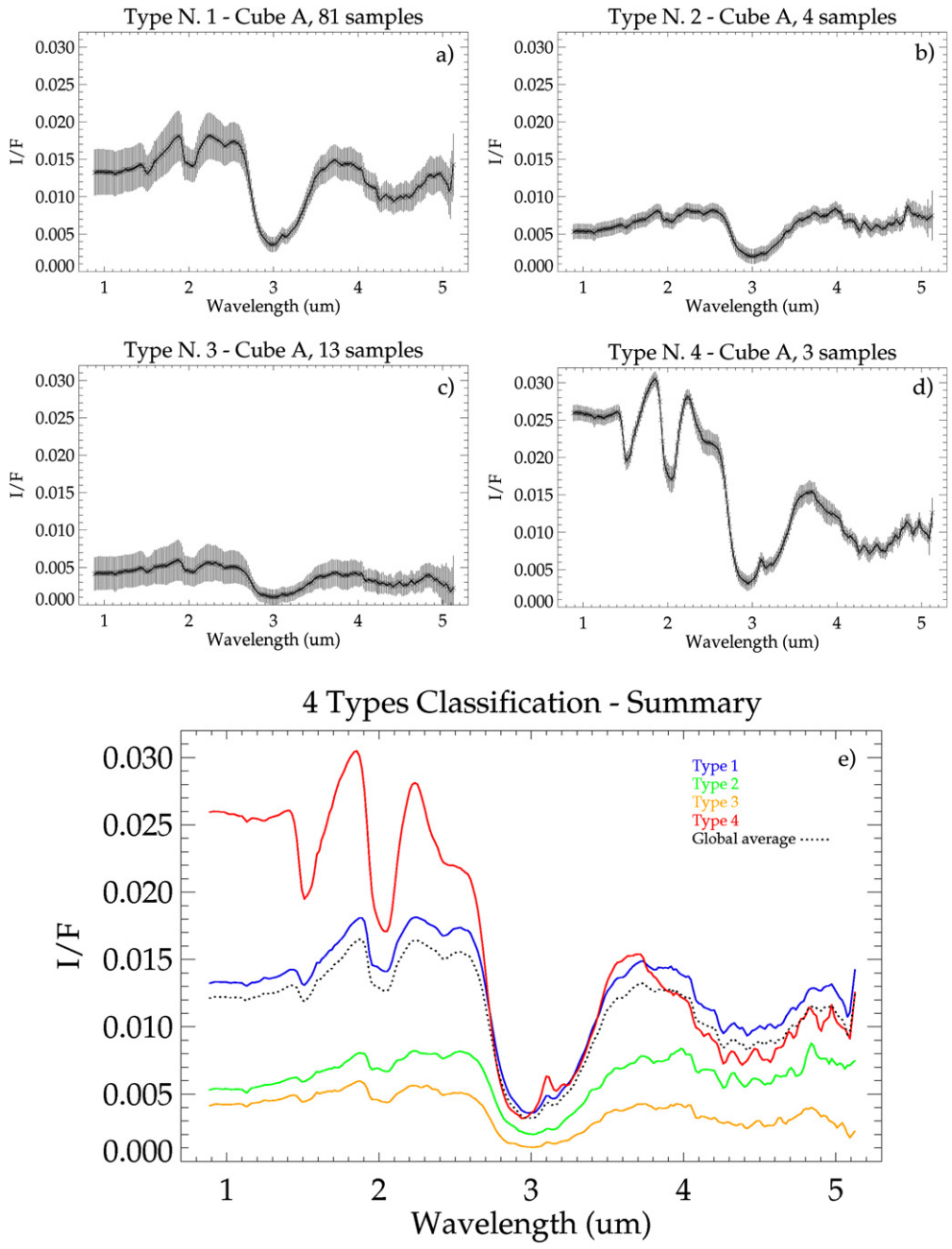

Fig. 3. (a) Type #1 includes 81 samples. These samples represent most of the satellite's image; they correspond to pixels with "average" illumination conditions, so we can consider them as a "background" spectrum of Phoebe. (b) Type #2 consists in 4 samples, corresponding to pixels of the image with very low I/F due to their closeness to the limb or to a crater's shaded inside wall. (c) Type #3 includes 13 samples, again with low I/F and spectrum showing a low abundance of CO_2, traced by the 4.26 μm absorption band. (d) Type #4 numbers 3 samples. These are a few pixels of the image with relatively high I/F and different continuum slope, due to the presence of exposed water ice. (e) Average I/F spectra of the 4 types isolated by the G-mode, using an absolute error of 0.001 and 99.0% confidence level, in the case of the application on the VIMS cube "A." The black dotted line represents the global average of all of the 101 samples.

following, "A," "B," "C," and "D," for the sake of brevity) acquired by VIMS during Phoebe closest approach. This subset was chosen in order to have, besides different spatial resolution, also different acquisition conditions, i.e., different integration times, geometries, operative modes, etc. In all of these cases, we have explored the PDS database in order to find simultaneous images by the ISS Narrow Angle Camera (NAC), which could serve as a convenient comparison. Table 2 gives details about these cubes.

5. Data analysis

5.1. Procedure

On all of the data discussed in this paper, the following procedure was applied. In the IR image, we selected all the pixels of the satellite with sufficiently high raw signal; thus, in this case, the dataset consists of N infrared spectra (pixels) of Phoebe acquired by VIMS-IR, each sampled in 256 wave-

lengths between 0.85 and 5.1 μm. Since we want to attempt an automatic mapping of the image, we keep the information about the position of every pixel inside the image.

All of the spectra were calibrated using the latest official VIMS-IR sensitivity function (Dyer, 2005, personal communication; for the VIMS calibration procedure see McCord et al., 2004), thereby converting the raw signal of each pixel of the target inside the IR image into radiance (divided by the IR integration time and the flat-field) and then into reflectance I/F, where I is the intensity of reflected light and πF is the plane-parallel flux of sunlight incident on the satellite (Thekaekara, 1973), scaled for its heliocentric distance. Then the spectra were "despiked": meaning we removed single-pixel, single-spectral channel deviations, caused by systematic instrumental artifacts like order-sorting filters as well as random artifacts like cosmic rays or high energy radiation striking the detectors (these events reveal themselves as spikes in the dark current stored in each cube) using an automatic procedure written in the IDL language (see Table 3). The spectra were finally organized into a text file, in order to be properly read by the G-mode program.

No illumination correction was applied to the spectra, because, given the irregular shape and rough topography of Phoebe, a 3D model reproducing the precise aspect of the satellite is needed, which was not available when we first analyzed these data. On the other hand, spectra with similar photometric characteristics are automatically classified in the same type by the G-mode, by taking into account, for each spectral channel (variable), not only the measured value of reflectance but also its deviation from the average value of a class, so that the spectral behavior of each class is peculiar with respect to the others.

Because of Phoebe's low albedo (maximum I/F is ∼0.08 in the VIMS-IR wavelengths), and its consequent low SNR, we initially assumed the same error for all of the 256 variables, so that the statistical weights of the variables would tend toward uniformity being comprised in the same order of magnitude (see Fig. 2). In principle, the actual instrumental error of each spectral channel of VIMS can be used as parameter by the G-mode. But since VIMS-IR has a larger instrumental error in the longer wavelengths, and the spectra of Phoebe show a large informative content in the range from 3.5 to 5.1 μm, we used an absolute statistic error, rather than the instrumental one, in order not to mislead the classification. Moreover, we deem this a more reliable approach in the case of a large statistical population like that offered by the VIMS data (more than 100 samples in each cube).

Table 4
Square root of the distance matrix computed by the program, for the 4-types classification of cube "A"

	Type #1	Type #2	Type #3	Type #4
Type #1	1.000	8.400	5.420	6.070
Type #2	8.400	1.000	4.550	4.060
Type #3	5.420	4.550	1.000	11.68
Type #4	6.070	4.060	11.68	1.000

5.2. Medium resolution data

VIMS data showing medium spatial resolution are extremely important since they give a general idea of the surface's spectral behavior; comparing them to the camera images allows us to correlate the spatial features with the large scale Phoebe geology. On the contrary, high-resolution cubes are in general scattered on the target, and not representative of the overall surface; they cannot be related to macroscopic geologic features but they do show peculiar signatures that are not seen on a global scale.

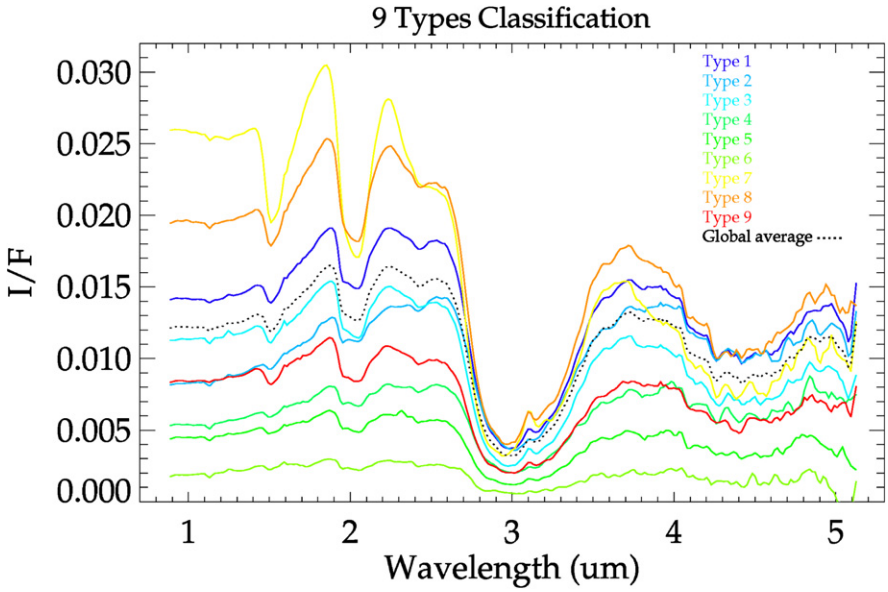

Fig. 4. Average I/F spectra of the 9 types isolated by the G-mode, using an absolute error of 0.001 and 96% confidence level, in the case of the application on the VIMS cube "A." The black dotted line represents the global average of all the 101 samples.

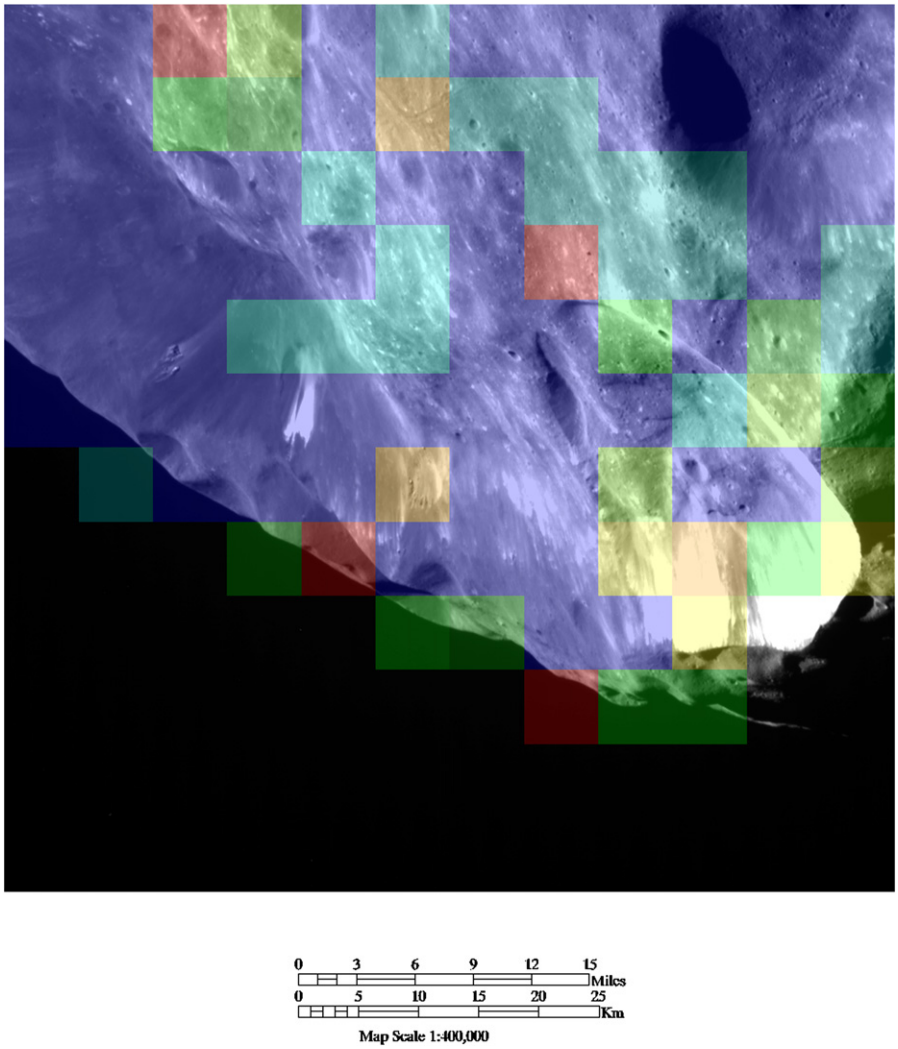

Fig. 5. Combined map of ISS NAC and infrared image taken from VIMS cube "A." The color code of the 9-types classification, shown in Fig. 4, is used. In this map, a smother degree of mixing between the dark and bright material is established.

We initially applied the method on the cube "A," acquired during the inbound phase of the flyby (see Table 2); Fig. 1 shows an infrared image extracted from this cube, coupled with a simultaneous image taken by the ISS NAC. The area visible in the image (center Lat = 24°.608, Lon = 329°.218) corresponds to crater Erginus, a geological feature located on the border of the 100-km crater Jason, according to the naming scheme proposed by the Cassini imaging team (Porco et al., 2005).

Assuming 99.0% confidence level, the classification leads to 4 types. The first type has 81 samples, whereas the other types have 4, 13 and 3 samples, respectively. In Fig. 3, we show the average spectra (i.e., mean values of the variables) of each type, allowing (eventually) an interpretation. Error bars (i.e., standard deviations of the variables) are computed by the G-mode and are shown, as well. At the bottom of the image, a synthesis of these average spectra is provided.

One sees that the higher the homogeneity of the group, the smaller its deviation from the average. Thus type #1 is very homogeneous despite the large number of samples characterizing it, the average standard deviation being less than 0.004 (Fig. 3a). Also types #2 and #4 are extremely well defined, with $\sigma < 0.003$ and $\sigma < 0.002$, respectively (Figs. 3b and 3d), whereas type #3 appears relatively less homogeneous ($\sigma > 0.004$, in Fig. 3c). It is worthwhile to note that the average spectra of the classes have a low level of noise. Thanks to the clustering method, that automatically enables one to cluster similar samples together, the average is strongly representative of the class behavior. This allows a confident interpretation of the long-wavelength portion of the spectrum, characterized by a high instrumental noise. This portion is extremely important in discriminating among classes due to its high information content, as discussed later.

The comparison between the average spectra (Fig. 3e) shows that the differences among types are clear and that our automatic classification, in general, is in agreement with the identification of different types reported in Fig. 2 of Clark et al. (2005).

Through the information on the spatial positions of the spectra, it is possible to correlate the position of each multispectral pixel of VIMS with the identification of the group, thus au-

tomatically reconstructing a spectral map of the image (see Fig. 1).

The broad classification obtained with a high confidence level shows that only a few types are discriminated by the G-mode, but these are significantly different one from another: the distance matrix, computed at the end of the processing and representing the statistical distances of each type with respect to the others on the basis of all the meaningful variables, shows that the major differences are between type #3 and #4, and between types #1 and #2 (see Table 4).

Type #1 (in blue) collects most of the pixels of the satellite's image, and it is actually close to the spectrum represented by the global average of all the samples. This confirms the fact that the Phoebe's surface is essentially homogeneous from a spectrophotometric point of view, except for some spots that are actually classified into other types. Types #2 and #3 (green and yellow, respectively) correspond to pixels with low illumination conditions, located close to the limb or to the crater Erginus' rim; however they differ in the longer wavelength portion of the spectrum between 4 and 5 μm. Type #4 (red) is the most peculiar in this classification: this cluster is representative of a few pixels of the image relative to an area of the satellite where exposed water ice appears and the dark terrain seems to have slid away, as suggested both by a comparison with the ISS NAC image and by the spectral trend (slope of the continuum in the range between ∼1.0 and 2.6 μm, 2.0 μm band shape, 3.1 μm peak), typical of "clean" water ice. Moreover, in this type a signature at 3.25 μm, discussed in the next paragraph, appears more defined than in the other types.

By lowering the confidence level of the test, more types are found, as expected. For example, adopting 96% confidence level, the classification leads to nine types, whose average spectra are summarized in Fig. 4, and mapped on the IR image in Fig. 5.

Examining the nine types, it can be seen that type #7 (yellow) matches former type #4 (red in the 4-types classification obtained with 99% confidence level), thus representing pixels in which, thanks to the comparison with the image, exposed water ice can be recognized. In this finer classification, type #8 (orange) also shows the absorption features typical of water ice, but here the continuum slope is less steep than in type #7 and the absorption at 3.25 μm becomes an inflection. Type #1 (blue) still shows a certain amount of water ice—inferred from the absorption band shapes at 1.5 μm and 2.0 μm—even though the continuum slope is flatter, thus indicating a greater degree of mixing with the dark material. Types #4, #5 and #6 (dark, medium and light green, respectively) are low I/F types, mainly located on the rim of crater Erginus; these spectra are indicative of dark material, which has probably been exposed to space for a long time. Types #2 and #3 (dark and light cyan, respectively), located again on the rim of crater Erginus and in the middle of crater Jason, represent an intermediate situation, even though these two types show a different continuum trend in the range from 1.0 to 2.6 μm.

In what follows, diagnostic spectral features evidenced by our G-mode classification are discerned and compared with those already proposed by Clark et al. (2005). Although the discussion refers to the cube "A," it can be extended to the other cubes with similar spatial resolution.

In order to focus the discussion, a more detailed analysis will be performed on three spectral zones from Fig. 3e, covering the 0.85–2.70, 2.70–3.50 and 3.50–5.1 μm ranges, respectively.

In the following plots, the wavelengths corresponding to the VIMS-IR's order-sorting filters (typically involving a few spectral channels) are not shown, because in these positions a despiking procedure was systematically applied in order to remove instrumental artifacts. Other temporary malfunctions occurred during the Phoebe flyby, particularly the blinding of some spectral channels, are emphasized as well. Again, in these

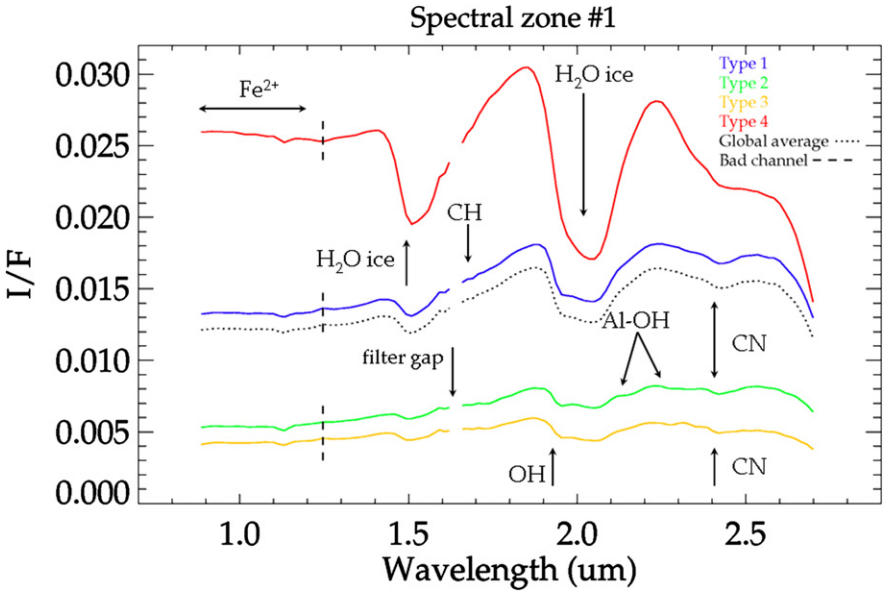

Fig. 6. Detail of the G-mode classification on the cube "A" in the 0.85–2.70 μm range. The wavelengths affected by the 1.64 μm order-sorting filter are not shown. A vertical dashed line at 1.25 μm indicates the position affected by a 'hot' spectral channel, where a despiking procedure was applied.

positions, single-channel spikes were identified and removed, so the corresponding wavelengths (listed in Table 3) will not be considered for the interpretation.

The first region (Fig. 6) is dominated by the spectral features of water, which is ubiquitous on Phoebe. Here we mainly have water of hydration or hydrated minerals, i.e., "bound" water (revealed by the 1.95 and 3.0 μm signatures), but sometimes water appears also in the form of ice (whose signatures occur at 1.04, 1.25, 1.50, 2.02 and ∼3.0 μm, increasing in strength with increasing wavelength), already identified by telescopic observations (Owen et al., 1999). Another recurrent feature is the broad Fe^{2+} absorption, located at the shortest VIMS-IR wavelengths (0.85–1.2 μm); this absorption is related to phyllosilicates rather than to pyroxenes (Clark et al., 2005). The 1.69 μm feature is likely to be ascribed to a CH stretch overtone. Other small features (which tend to disappear in the water ice) can be seen at ∼2.15 (inflection on the right wall of the water absorption), ∼2.33 and ∼2.42 μm. The first two could be related to Al–OH (actually, the 2.33 μm feature could be an overtone of the CN fundamental stretch, as well) and are also consistent with phyllosilicates (Clark et al., 2005). The ∼2.42 μm feature, visible in many spectra, has been attributed to a cyanide compound (Clark et al., 2005). The position of the minimum of this band can appear slightly shifted from area to area, sometimes occurring at ∼2.44 μm. In this case the signature position depends on the atom, molecule or group attached to the CN; in particular, KCN best fits the 2.42 μm position, although other counterparts could be responsible as well (Clark, 2007, personal communication).

In the second interval, ranging from 2.70 to 3.50 μm (Fig. 7), all of the classes of spectra are dominated by the large ∼3 μm absorption band due to the asymmetric OH stretch, which does not appear fully saturated since some weak features are still recognizable (often appearing as inflections) in the band itself. Because this behavior is seen also in the Iapetus' dark side data (Buratti et al., 2005; Cruikshank et al., 2007), whereas for Enceladus this band appears always saturated even at the shortest IR exposure times (Brown et al., 2006), it can be inferred that the band does not saturate when the satellite's average albedo is very low.

The Fresnel reflection peak, typical of water ice and snow, dominates the spectrum at 3.1 μm. This peak comes from reflection by the surface grains; its shape and strength do not depend strongly on the grain size but rather on the number of grains and, therefore, in principle it could yield an estimate of the surface ice abundance (Hansen, 2002). The feature located at 2.85 μm is a standard assignment of the OH stretching vibrational fundamental; it actually appears as an inflection within the 3 μm absorption band. The ∼3.25 μm feature, although close to a 'hot' spectral channel, is likely to be the spectral counterpart of the aromatic CH stretch (maybe due to the presence of polycyclic aromatic hydrocarbons, PAHs). This feature is more evident in type #4, i.e., in the pixels corresponding to exposed water ice, while in the other types it is only recognizable as an inflection, suggesting that the responsible compound is related to bright material. The feature appearing at 3.4 μm (evident in type #2) can be interpreted as the signature of the CH stretch fundamental (anti-symmetric mode); this interpretation supports the presence of another weak absorption feature, visible only in low I/F types, located at 3.53 μm and possibly due to the aliphatic CH stretch (symmetric mode), which was not reported by Clark et al. Again, these two features are recognizable as inflections, whereas they tend to take a more definite shape in the low I/F types.

The third region, ranging from 3.50 to 5.1 μm (Fig. 8), is possibly the most interesting from the point of view of compositional information; here, VIMS spectra show the presence of several features seen only on Phoebe.

The first spectral signature in this range is visible at 3.6 μm. Clark et al. (2005) pointed out that this could be a peculiar fea-

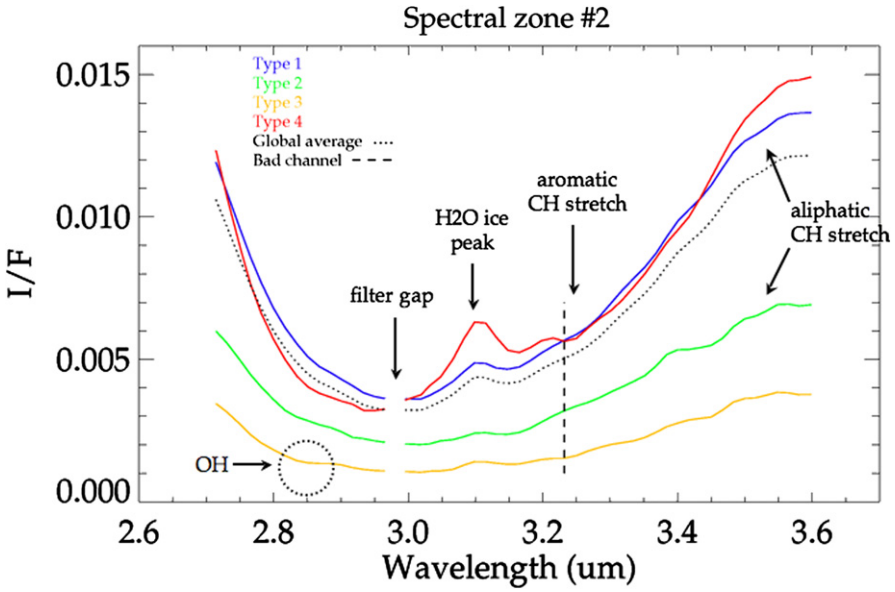

Fig. 7. Detail of the G-mode classification on the cube "A" in the 2.70–3.50 μm range. The wavelengths affected by the 2.98 μm order-sorting filter are not shown. The vertical dashed line at 3.23 μm indicates the position affected by a 'hot' spectral channel, where a despiking procedure was applied.

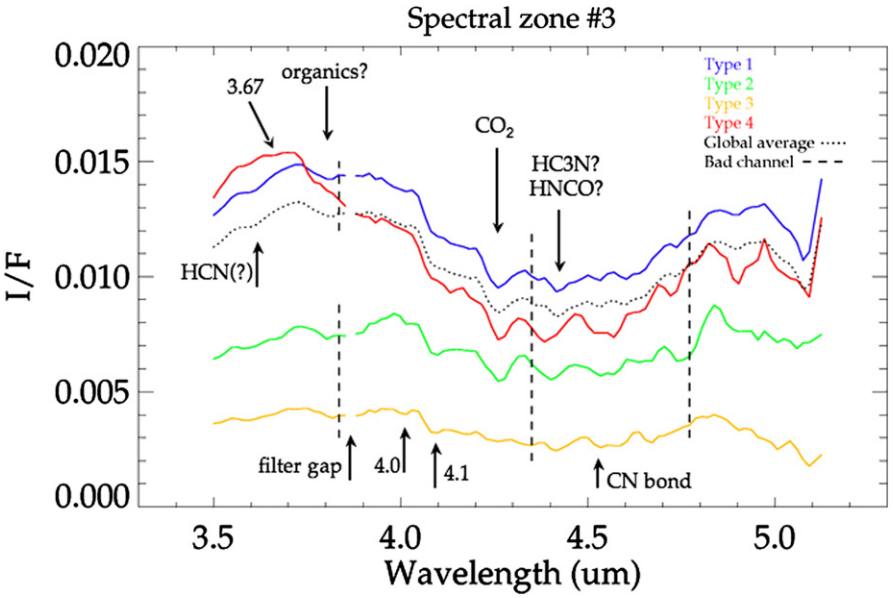

Fig. 8. Detail of the G-mode classification on the cube "A" in the 3.50–5.1 μm range. The wavelengths affected by the 3.87 μm order-sorting filter are not shown. The vertical dashed lines at 3.84, 4.35 and 4.77 μm indicate the positions affected by 'hot' spectral channels, where a despiking procedure was applied.

ture of HCN (in this case a major absorption, due to the CH stretching fundamental, is expected at 3.02 μm, which cannot be seen due to the large 3 μm water band). Another weak feature appears at 3.67–3.68 μm; it was not reported before and it mostly appears as an inflection in low I/F types. The next signature is seen at 3.8 μm. This feature, almost invisible in high I/F types, appears located inside another broader (∼0.2 μm width) feature. Although close to some unreliable VIMS-IR's spectral channels, this feature has been interpreted as real and organic-related (Clark et al., 2005). On the other hand, a weak signature taking place at ∼4.0 μm, followed by another feature at 4.1 μm (again, more evident in the case of lower I/F types), were not reported before. The 4.26 μm absorption is a standard assignment of CO_2, which is ubiquitous on Phoebe, although more spatially variable than water ice (Clark et al., 2005). Its wavelength position and shape are similar to that of the trapped CO_2 found on Callisto and Ganymede (McCord et al., 1998).

An absorption feature at ∼4.4 μm was not reported before and may be caused by a cyanide compound such as HC_3N. Alternatively, a comparison of this band with laboratory spectra (Strazzulla, 2005, personal communication) suggests that it could be due to the superposition of three components: HNCO (peaked at 4.42 μm), $^{13}CO_2$ (peaked at 4.39 μm), and NO_2 or a suboxide, namely C_3O_2 (both peaked at 4.47 μm).

On the surface of Phoebe, the triple CN bond is recurrent and revealed by the narrow absorption at 4.53–4.55 μm (again, the detailed wavelength position of this signature can change depending on the compound's specific composition), although the relative depth of this band can change from type to type. This justifies the presence of the other absorptions already seen at 2.42, 3.6 and 4.4 μm; yet an identification of the actual mixture is not trivial. The weak feature at 3.6 μm may be indicative of HCN, but other compounds could be present. The signature located at ∼4.67 μm could be an instrumental artifact; or, in principle, it could be related to CO. The presence of CO ice is unlikely, due to typical temperatures of Phoebe inferred by the Cassini/CIRS instrument to range from ∼70 to 112 K (Spencer et al., 2004). Nevertheless, the CO could be dissolved in water ice (for example, in a clathrate structure, mixed in amorphous ice or trapped in grain boundaries and dislocations). Beyond 4.7 μm, other absorption features occur, appearing at non-unique wavelengths (i.e., shifted from type to type): they could be artifacts due to instrumental noise and/or to the despiking procedure. Although VIMS-IR' SNR is low in this region, these signatures are seen in many cubes of Phoebe, so they could be the counterparts of real compounds.

It is interesting to note that if the new identification here proposed, namely the presence of sub-oxides or N-bearing oxides, is correct, it reinforces the statement by Clark et al. (2005) that Phoebe's organic and cyanide compositions are unlike any surface yet observed in the inner Solar System. Both the overall low albedo and the composition inferred here (in particular CN bonds and suboxides) could be produced by cosmic rays bombardment of a surface originally dominated by simple ices (see Strazzulla et al., 2003).

As a further test on the average spectra found by the G-mode, the strengths of some spectral signatures were computed for the classified types. To estimate the band strength, we followed the definition by Clark and Roush (1984):

$$D = 1 - \frac{R_b}{R_c}, \tag{1}$$

where R_c is the reflectance of the spectral continuum (reconstructed through a linear fit) at the band center, and R_b is the reflectance measured at the band center. By making the same computation for another type for a given absorption band, from the ratio of the two strengths, a proper band ratio can be obtained. Furthermore, it is also possible to plot the values of the strengths for all the types, over a larger set of absorption bands, thus allowing both a comparison of the abundance of a given

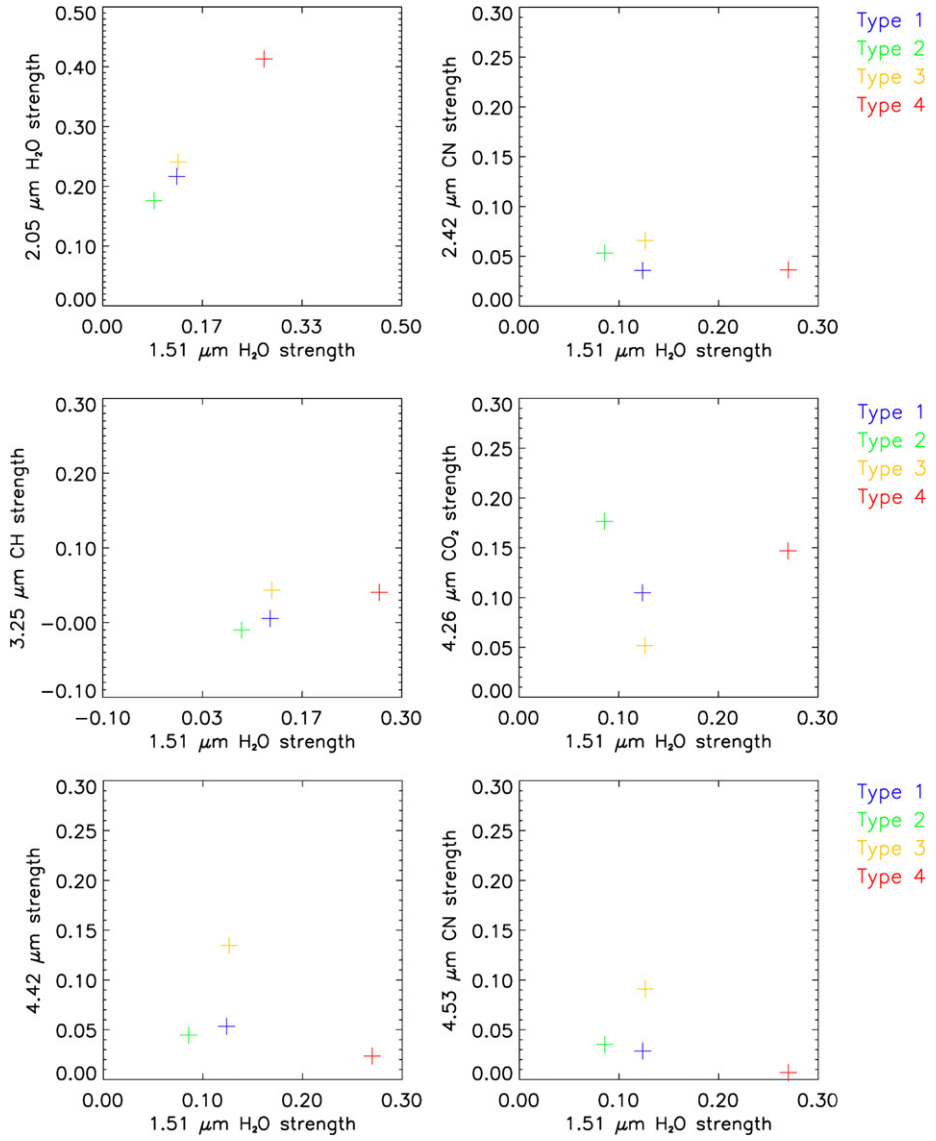

Fig. 9. Band strengths of some diagnostic spectral signatures with respect to the 1.51 μm water ice signature strength, computed for the 4-types classification in cube "A." The color code of Figs. 1 and 3e is used.

compound between different types, and an evaluation of the trend of the abundance of different compounds for a given type. In our case, this has been done for some diagnostic spectral signatures with respect to the 1.51 water ice signature (Figs. 9 and 10).

By using these signatures as "markers," in the case of the cube "A," with the 4-types classification (see Fig. 9) a general trend can be observed, with CO_2 content increasing with exposed water ice (see type #4, red). Also aromatic hydrocarbons (revealed at 3.25 μm) seem to be more abundant where water ice is exposed (see types #3 and #4, in yellow and red, respectively).

On the contrary, the strengths of the CN bond (revealed both at 2.42 and 4.53 μm), as well as the strength of the ∼4.4 μm feature, do not show any clear correlation with exposed ice, whereas they are larger in type #3 (yellow), located on the rim of crater Erginus. This latter type also shows the stronger strengths for the 4.0 and 4.1 μm signatures. Eventually, type #1 (blue) shows similar abundances of these compounds (see Table 5). This is also consistent with the higher statistical distance—giving a measure of the differences among classes—characterizing types #2 and #4 with respect to type #1, which is close to the global average of all the samples.

Table 5
Estimated band strengths of water ice, CO_2, aromatic CH and CO_2, and H_2O:CO_2 and H_2O:CH ratios, for the 4-types classification of cube "A"

	Type 1	Type 2	Type 3	Type 4
H_2O	0.124	0.086	0.126	0.270
CO_2	0.105	0.176	0.052	0.147
Arom. CH	0.005	−0.010	0.043	0.041
H_2O:CO_2	1.180	0.485	2.444	1.838
H_2O:CH	22.599	−8.541	2.923	6.657

Moving to the 9-types classification (Fig. 10), types #4 and #7 (sea-green and yellow, respectively) exhibit the highest abundance of CO_2; in the case of type #4, located on the rim of

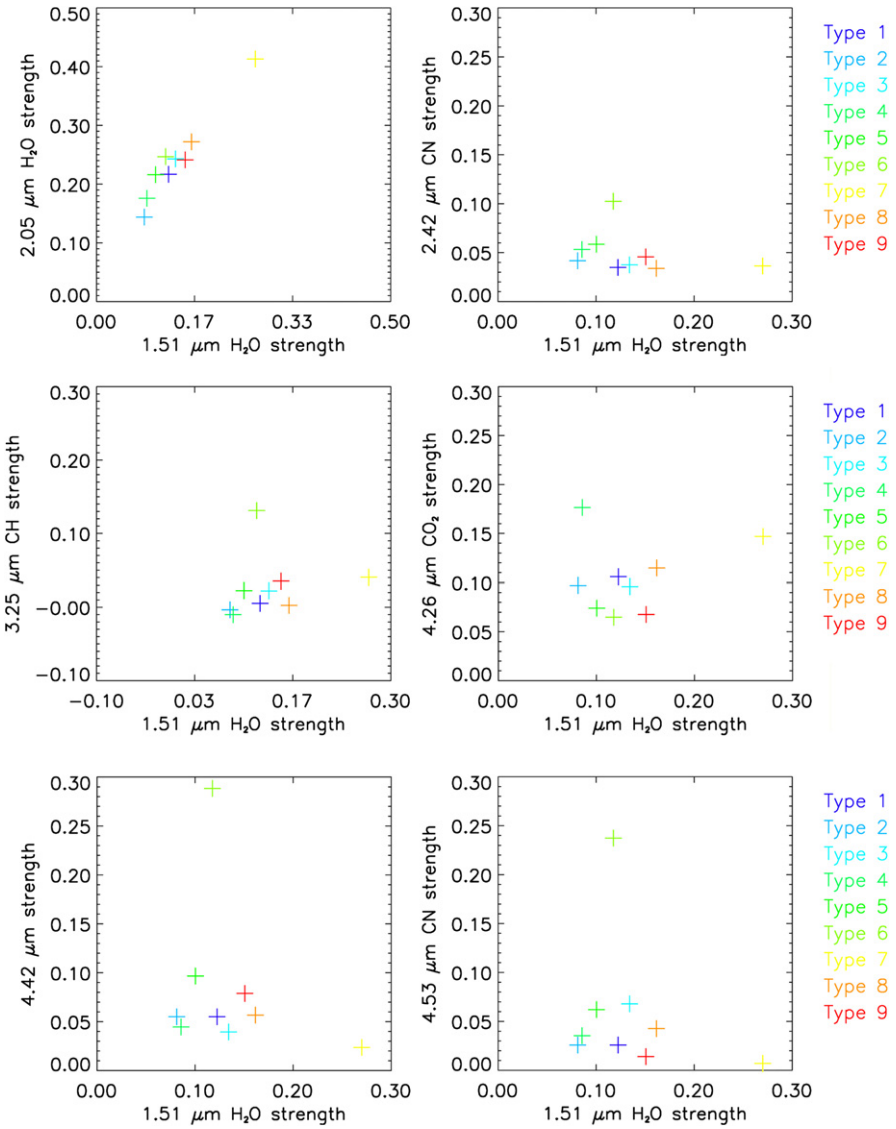

Fig. 10. Band strengths of some diagnostic spectral signatures with respect to the 1.51 μm water ice signature strength, computed for the 9-types classification in cube "A." The color code of Figs. 4 and 5 is used.

crater Erginus, there is no evident relation with of the CO_2 with water ice. Type #6 (light green) shows a low content of CO_2, whereas it shows the major abundance of cyanide compounds. Types #2 and #3, located on the center and rim of crater Jason, represent an intermediate situation, with an average amount of volatile weakly related to water ice.

In this classification, we can see that the transition from high-volatile areas to volatile-depleted areas is not as clean as in the 4-types classification, but indeed rather smooth: the analysis shows that, when the dark veneer that appears to cover the surface is removed by some event (e.g., an impact), ices with rich in carbon dioxide and organics are exposed.

A second analysis on medium resolution data was performed by the application of the G-mode method to the cube "B" (see Table 2). In this case, the classification appears very stable, scarcely affected by the confidence level: a few types are found if a high confidence level is kept. This indicates that the classification is mainly affected by the errors, due to the fact that the statistical weights of the variables encompass a few orders of magnitude, so the classification itself is performed by using a small set of spectral channels (Tosi et al., 2005). For instance, assuming 97.5% confidence level, only 2 types are found, the first being by far the largest (475 samples). In Fig. 11, the two average spectra are superimposed without error bars, in order to help the comparison; their location is overlapped on a simultaneous ISS camera image in Fig. 12 (center Lat = 15°.438, Lon = 298°.164).

As in the previous cube, the 2 types have similar I/F levels, indicating that differences cannot be simply related only to peculiar illumination conditions. Type #1 (cyan) almost perfectly matches the global average of all the samples. On the other hand, the continuum slope and the shape of the 2.0 μm band in type #2 (red) again appear compatible with a larger amount of water ice, consistently with the location of this spectral unit on the rim of crater Erginus. This type also shows a higher content of organics, revealed by the inflections at 3.25

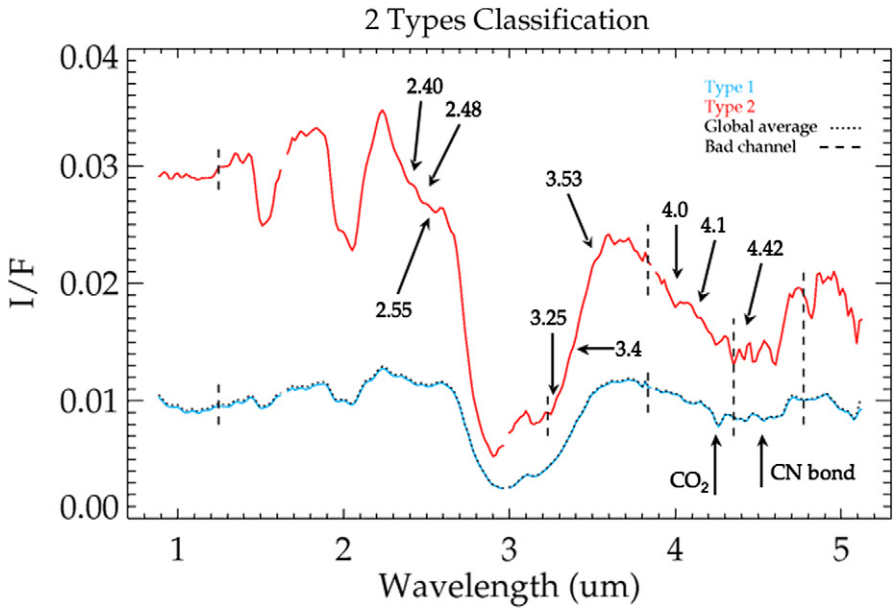

Fig. 11. Summary of the 2 types found applying the G-mode on the cube "B," using an absolute error of 0.001 and 97.5% confidence level. The black dotted line represents the global average of all the samples.

and 3.53 μm feature possibly related to hydrocarbons. Also the 4.0 μm signature is stronger in this type, whereas it tends to get lost in type #1, which, on the contrary, shows the 4.1 μm feature. Furthermore, in type #2 the 2.42 μm CN feature is actually seen at 2.40 μm, whereas new features can be seen at 2.48 and 2.55 μm; these signatures, disappearing in the global average, were not reported before and are still to be interpreted.

5.3. High-resolution cubes

Cube "C" was first selected to test the G-mode method on high-resolution data (see Table 2). Here there are no sky background pixels since the satellite's surface fills the FOV, thus for the classification we considered all of the 144 pixels composing the image. Fig. 14 combines an IR image taken from this cube and an ISS image, showing an area with a nameless crater (center Lat $= -12°.176$, Lon $= 6°.776$).

In this case, assuming 99.8% confidence level, the G-mode classification has the capability to extract 3 types from the Phoebe's "background" spectrum. A summary of these classes is shown in Fig. 13, while Fig. 14 indicates their location superimposed on a simultaneous NAC image.

These types show a similar I/F level and a similar continuum slope, so they are not trivially due to different illumination conditions induced by the topography, nor to freshly exposed water ice.

Type #1, in cyan, represents most of the samples, including the crater feature visible in foreground (except for two pixels); types #2 and #3, shown in green and red, respectively, correspond to pixels surrounding this crater. From the spectral summary shown in Fig. 13, it can be seen that type #2 (green) is characterized by a very low I/F. On the basis of the bands strengths' computation, it is found that this type shows the highest amount of organics and cyanide compounds. Type #3 (red) shows a slightly higher content of CO_2, and also the 3.25, 3.4 and 3.53 μm features (various CH stretches) are stronger with respect to the global average of all the samples, suggesting that these pixels correspond to a higher content of hydrocarbons. It can be noticed that types #1 (cyan) and #3 (red) show the presence of the 4.0 and 4.1 μm features (the latter being stronger in type #3) as well as two features at 2.22 (not reported before) and 2.55 μm. Moreover, in all of the three types, the CN band is actually found at 2.44 μm, the 4.35 μm signature is probably an artifact of the despiking, and the ∼4.4 μm band is found at 4.47 μm. It should be mentioned that in this cube, by decreasing the confidence level from 99.8% to 99.5%, type #3 (red) could be further split in two groups, characterized by slightly different strengths of the 2.15 μm (Al–OH) and 4.26 μm (CO_2) features.

After this classification, we reclassified only the largest of these types: type #1 (cyan in Figs. 14 and 13), consisting in 82 samples. Again, this was performed by keeping an absolute error of 0.001 on the variables and trying several confidence levels. In the range between 99.0% and 99.5% confidence level, we always find 3 subtypes; the first of these subtypes is always the largest. Fig. 15 shows a summary of the average spectra relative to these subtypes, while Fig. 16 reveals their location overlapped on the NAC image.

A larger statistical distance is found in this case between subtypes #1 and #2, because of many differences involving both the I/F level and the shape of the absorption bands. Subtype #1 (blue) is related to very low albedo material. Subtype #3 (red) shows a higher content of organics (revealed by the 3.25 and 3.4 μm features) and cyanide compounds (revealed by the strengths at 2.44 and 4.53 μm), which, although not easily linkable to any geologic feature, seem to be concentrated near the crater. On the other hand, the 4.0 μm signature is stronger in subtype #2 (green), whereas the 4.1 μm feature is stronger in subtype #1 (blue).

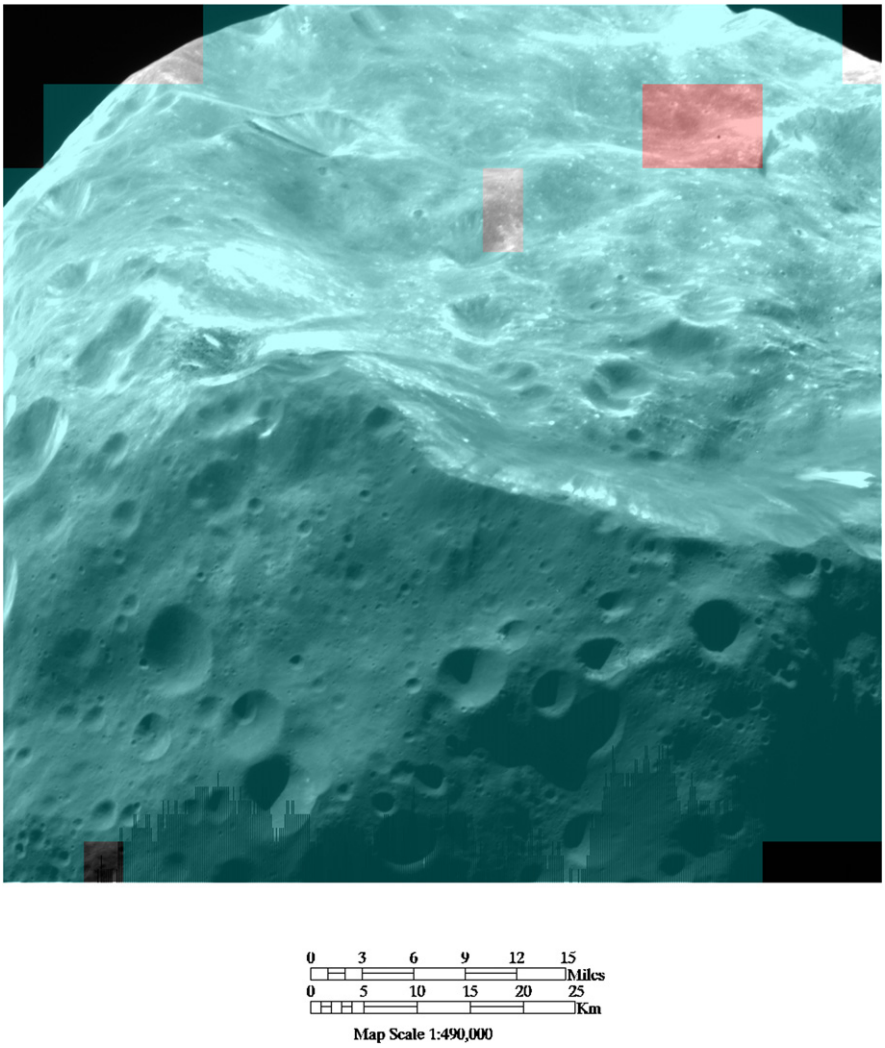

Fig. 12. Combined map of ISS NAC and infrared image taken from VIMS cube "B." The original field of view of this VIMS cube ($0.92° \times 0.52°$) was cut to properly overlap the $0.35° \times 0.35°$ NAC FOV. The color code of the average spectra shown in Fig. 11 is used. The colorless pixels are relative to spectra discarded by the processing.

A second analysis on high-resolution data was performed on cube "D." This is one of the VIMS acquisition of Phoebe characterized by the best spatial resolution, since it was taken during the closest approach phase, with the spacecraft ∼2480 km away from the satellite (see Table 2). Fig. 18 shows an area (center Lat = 1°.485, Lon = 327°.851) located in crater Jason.

Again, we applied the G-mode on the IR portion of this cube assuming an absolute statistic error of 0.001 and several confidence level values. For example, assuming 98% confidence level, 4 types are found; the first type is made up of 90 samples, whereas the other types have 38, 10, and 5 samples, respectively. The average I/F spectra of these types are summarized in Fig. 17, and they are mapped on a simultaneous NAC image in Fig. 18.

Although the G-mode output gives, as usual, a first type (blue) containing a large number of samples (thus closer to the global average of all the samples), the other obtained types—consistently with the relatively low phase angle, 37.4°—seem not to be trivially attributable to low-lighting pixels of the image. Although they show a similar I/F level and similar concentrations of cyanide compounds (inferred from the strengths at 2.42 and 4.55 μm), some subtle differences can be pointed out, which are representative of crater Jason. For example, type #4 (red), which is quite homogeneous having average $\sigma = 0.025$, exhibits differences related not only to its spectral continuum slope, but also to the strength and shape of the water bands at 1.5 and 2.0 μm (suggesting a larger amount of water ice), coupled with the 1.7 μm CH overtone and the 3.25 μm aromatic CH signature. On the other hand, type #2 (green), located in the center image, shows the strongest strengths for the 4.26 μm CO_2 and 4.1 μm signatures, while type #3 (yellow), embracing a small crater in the upper right side of the image, shows again the 2.55 μm feature, as well as slightly larger strengths for the 4.0 and 4.4 μm features.

6. Conclusions

This work allows us to draw two general conclusions. The first is methodological and related to the general effectiveness of multivariate analysis for imaging spectroscopy data. By av-

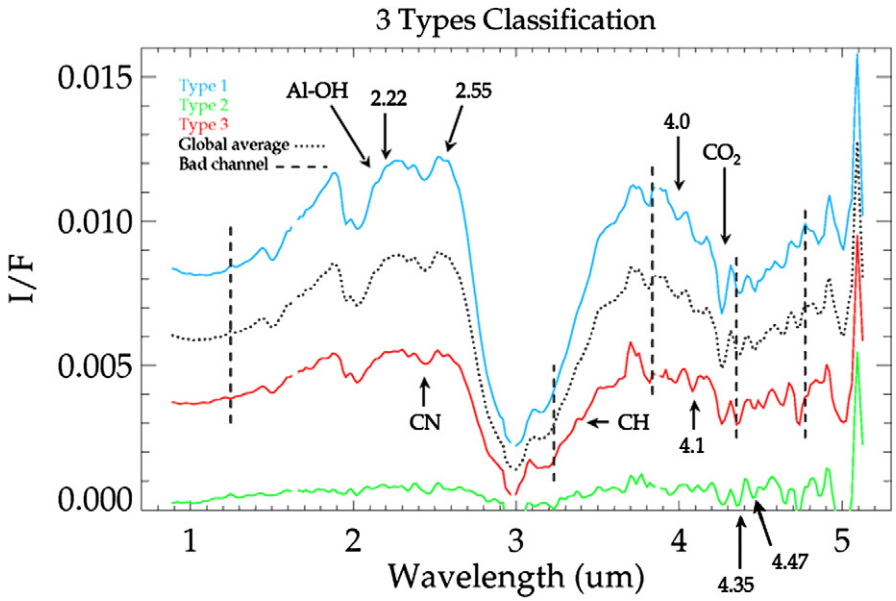

Fig. 13. Summary of the average I/F spectra relative to the 3 types found by the G-mode, using an absolute error of 0.001 and 99.8% confidence level, in the case of the application on the VIMS cube "C." The black dotted line represents the global average of all the 144 samples.

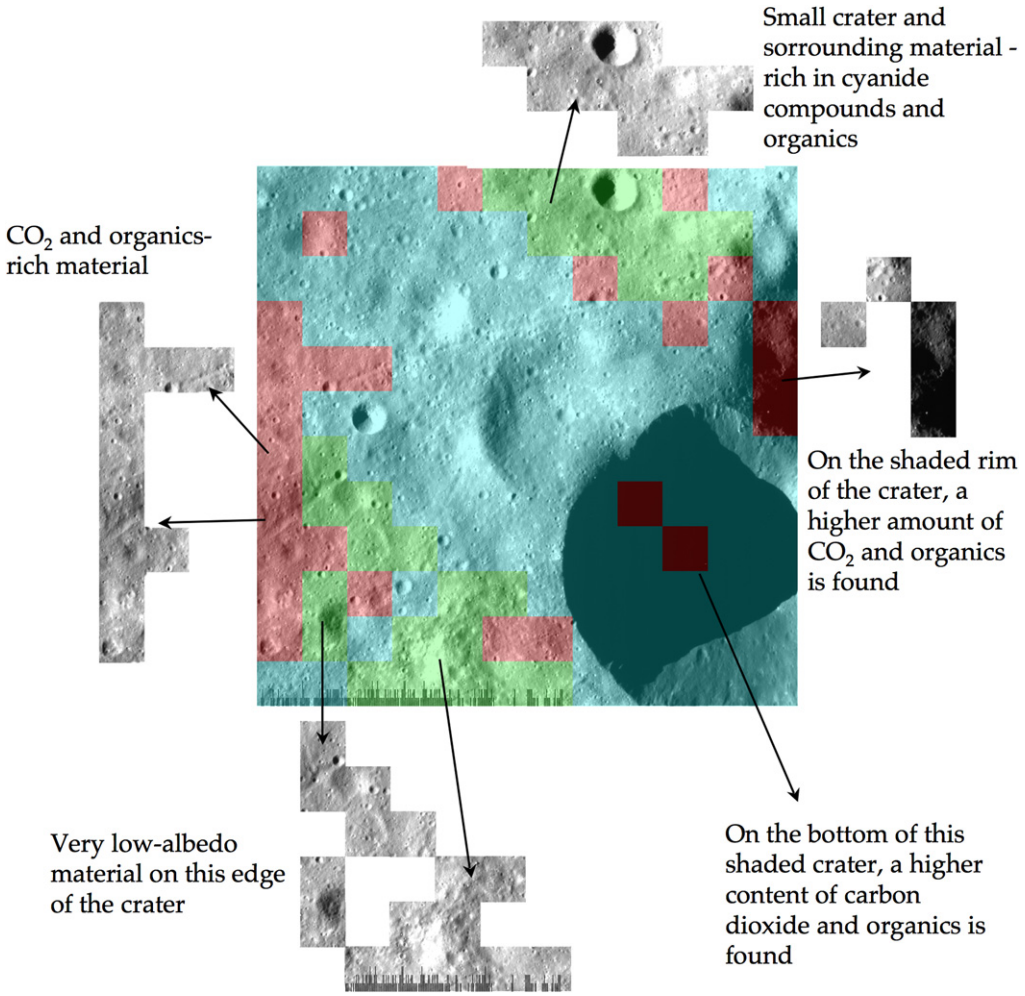

Fig. 14. Combined map of ISS NAC and infrared image taken from VIMS cube "C." The color code of the average spectra shown in Fig. 13 is used. A correlation with geology is better attempted by exploding the units outside the figure, without overlapping colors to the original image. In this map, cyan represents the typical surface composition of Phoebe, where bound water is abundant. The green class, very low in albedo, represents material rich in organics and cyanide compounds, ejected from the small crater in the upper side. The red class represents CO_2 and organics-rich material, relatively fresh and less affected by space weathering.

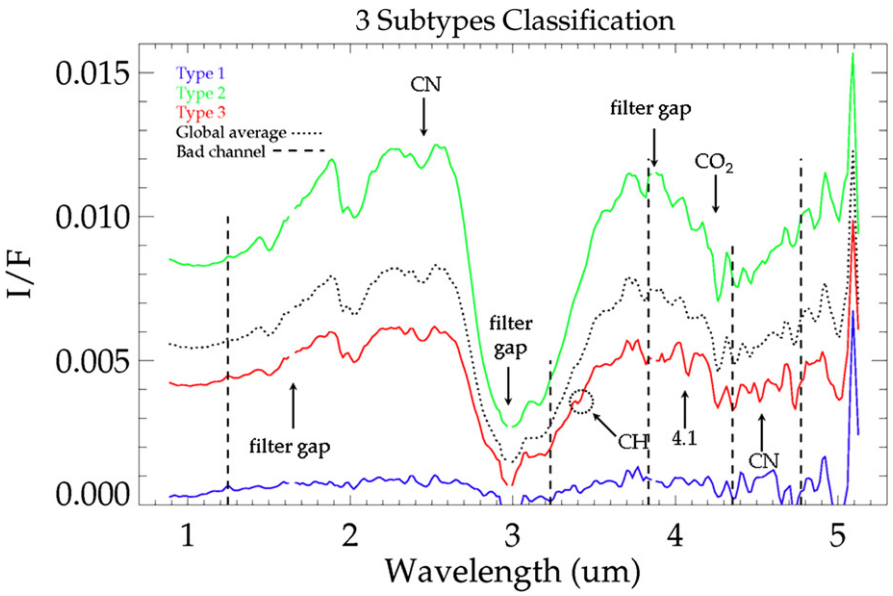

Fig. 15. Summary of the average I/F spectra relative to the 3 subtypes found by the G-mode, using an absolute error of 0.001 and 99.2% confidence level, in the case of the reapplication on the first type of the cube "C." The black dotted line represents the global average of the 82 samples.

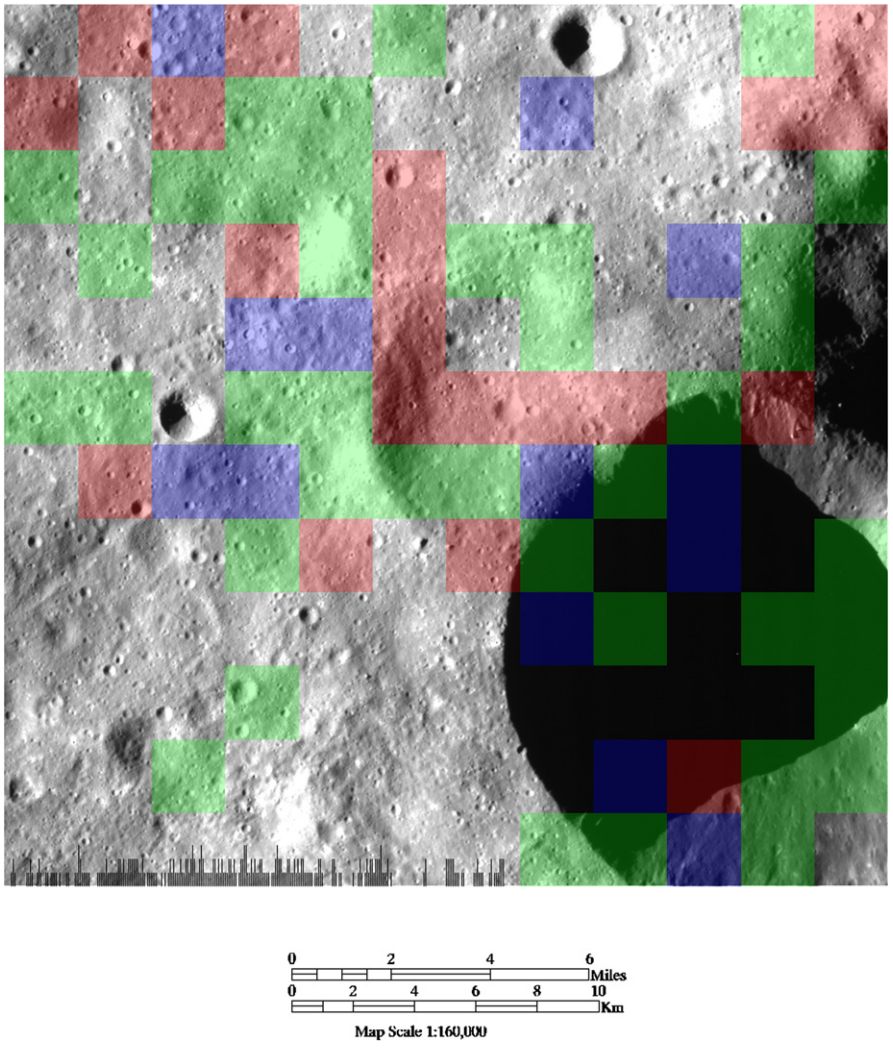

Fig. 16. Combined map of NAC and classified infrared image taken from VIMS cube "C." In this case, the G-mode method was reapplied on the first type only (cyan in Fig. 14), using an absolute statistic error of 0.001 and 99.2% confidence level. The color code of Fig. 15 is used.

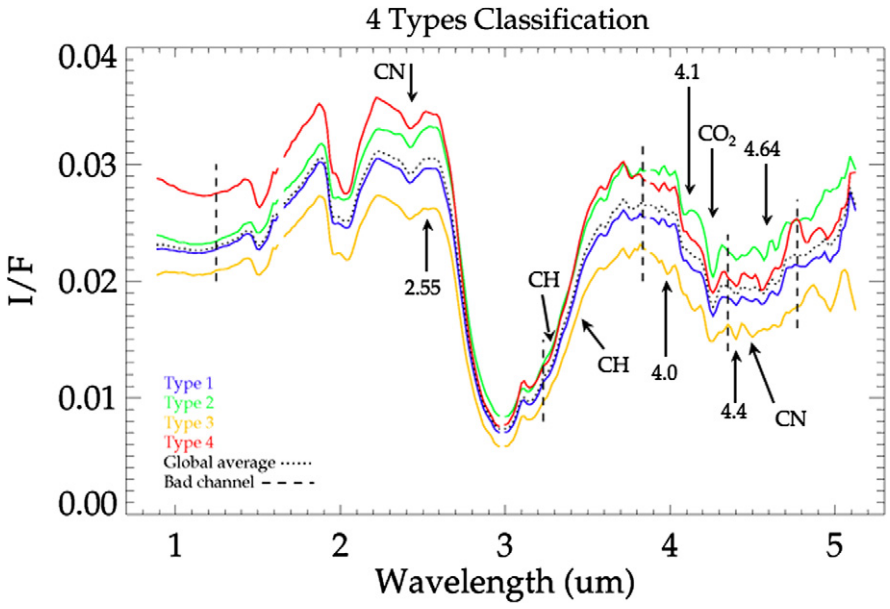

Fig. 17. Summary of the 4 types found applying the G-mode on the cube "D," using a statistic error of 0.001 and a 98% confidence level. The black dotted line represents the global average of all of the 144 samples.

Table 6
New spectral signatures on Phoebe pointed out in this work

Feature	Wavelength (μm)	Figure #	Note	Proposed origin
1	2.22	13	Weak and seen only in hi-res	?
2	2.48	11	Weak	?
3	2.55	11, 13, 17	Weak feature seen at different scales	?
4	3.53	7, 11	Seen as inflection in many cubes	Aliphatic CH stretch (?)
5	3.67–3.68	8	Weak inflection in low I/F types	?
6	∼4.0	8, 11, 13	Appearing at non-unique wavelengths	?
7	∼4.1	8, 11, 13, 15	Appearing at non-unique wavelengths	?
8	∼4.4	8, 13, 17	Appearing at non-unique wavelengths	Cyanide compound (HC_3N, HNCO?)
9	4.7	8	Appearing at non-unique wavelengths	Probable artifact

eraging too many samples (spectra) of the same target together, the SNR improves but the spectral information can get lost. On the contrary, a clustering method like the G-mode enables one to perform averages on samples not selected in a heuristic way, but which are statistically close each other on the basis of all the meaningful variables. In the case of Phoebe, some differences among the homogeneous types come out and weak spectral signatures can be highlighted, thus suggesting the presence of new compounds not reported before (particularly, the 3.53 μm signature, possibly due to aliphatic hydrocarbons, and the ∼4.4 μm signature, possibly associated with cyanide compounds), whose precise identification remains a task for the future (see Table 6).

One of the most interesting characteristics of the G-mode is its flexibility in the input settings: the user can explore different classifications by tuning both the errors on the variables and the confidence level of the statistical test. Furthermore, an aimed reclassification of a given type can be performed in order to look for subtypes characterized by subtle differences.

The second conclusion focuses on the results of our analysis. For the subset of VIMS data used in this work, the first type found by the G-mode always represents most of the pixels of the satellite's image, thus being closer to the global average. This is due in part to the fact that types extracted by the G-mode are dominated by the photometric level of the samples, as it is predictable since no illumination correction has been applied to the spectra. But it also implies that the composition of Phoebe is very homogeneous on a global scale, since the main signatures accounting for the chemical composition of the surface are seen in most of the VIMS pixels at any spatial resolution with different phase angles.

The use of a dataset characterized by both medium and high spatial resolution in principle can help quantify the extent of the spectral variability of the satellite's surface. We find that in medium resolution data the multivariate analysis can easily extract pixels of the image related to exposed ice, i.e., water ice that is not mantled or just partially coated by the dusty dark material, as observed in crater Erginus. In these pixels, the strengths of the absorptions due to CO_2 and aromatic hydrocarbons are stronger than in the rest of the satellite, suggesting that these compounds are associated with water ice. On the other hand, pixels where CO_2 is depleted show higher concentrations of cyanide compounds, and vice versa. However, this anti-correlation is not sharp, but rather smooth, with some regions showing an intermediate situation.

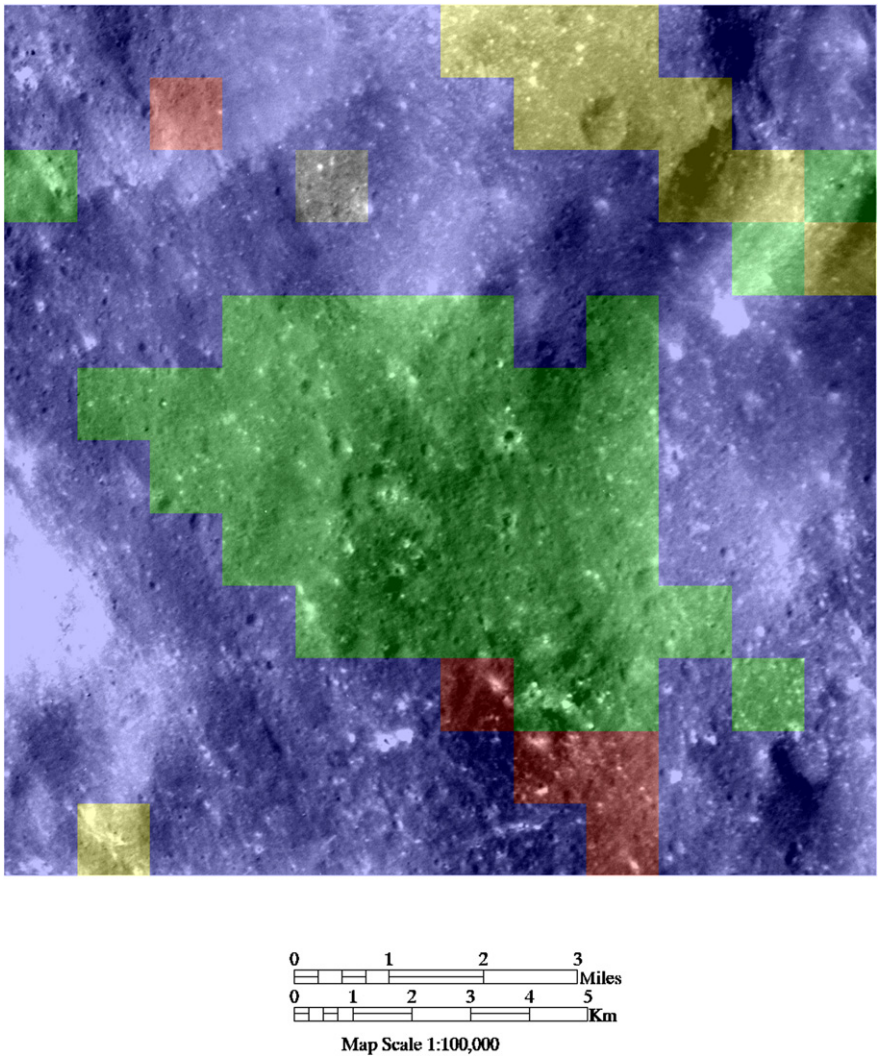

Fig. 18. Combined map of NAC and infrared image taken from VIMS cube "D." Different spectral types overlap geologic units. As usual, the blue class (largest) represent the background spectrum, i.e., the surface darkened by space weathering. The green class, rich in CO_2, corresponds to an area where the crust may have been removed. The yellow class almost overlaps the small crater on the upper right corner, and its ejecta blankets. The red class shows a trend similar to that of the green class, but with a higher water ice content.

In high-resolution data, showing smaller areas of Phoebe, the surface is rather homogeneous from a spectral point of view. The correlation of spectral units with geologic features is less immediate, because it is observed that spectral units are basically represented by a few samples, which sometimes may be scattered in the image. These units still show different concentrations of carbon dioxide, hydrocarbons and cyanide compounds on a local scale, even though the anti-correlation between the CO_2 and the cyanide compounds is not as evident as in the case of medium resolution cubes.

The presence of carbon dioxide and hydrocarbons associated to water ice, as well as the presence of cyanide compounds, provides direct constraints on the composition and state non-water-ice compounds in primitive bodies of the outer Solar System.

A successive work will be concerned with the G-mode analysis of the spectra of Phoebe, Iapetus and Hyperion together, the goal of which is to automatically look for similarities among the surfaces of these bodies.

Acknowledgments

This work was supported by the Italian Space Agency, ASI-INAF Grant I/031/05. We thank Dr. Carolyn C. Porco for providing the raw images acquired by the ISS Narrow Angle Camera, used in this paper. We also thank Dr. Jessica M. Sunshine for giving us many suggestions to improve the quality of this paper.

References

Barucci, M.A., Capria, M.T., Coradini, A., Fulchignoni, M., 1987. Classification of asteroids using G-mode analysis. Icarus 72, 304–324.

Bauer, J.M., Buratti, B.J., Simonelli, D.P., Owen, W.M., 2004. Recovering the rotational light curve of Phoebe. Astrophys. J. 610, L57–L60.

Bianchi, R., Coradini, A., Butler, J.C., Gavrishin, A.I., 1980. A classification of lunar rock and glass samples using the G-mode central method. Moon Planets 22, 305–322.

Brown, R.H., Baines, K.H., Bellucci, G., Bibring, J.-P., Buratti, B.J., Capaccioni, F., Cerroni, P., Clark, R.N., Coradini, A., Cruikshank, D.P., Drossart,

P., Formisano, V., Jaumann, R., Langevin, Y., Matson, D.L., McCord, T.B., Mennella, V., Miller, E., Nelson, R.M., Nicholson, P.D., Sicardy, B., Sotin, C., 2004. The Cassini Visual and Infrared Mapping Spectrometer (VIMS) investigation. Space Sci. Rev. 115, 111–168.

Brown, R.H., Clark, R.N., Buratti, B.J., Cruikshank, D.P., Barnes, J.W., Mastrapa, R.M.E., Bauer, J., Newman, S., Momary, T., Baines, K.H., Bellucci, G., Capaccioni, F., Cerroni, P., Combes, M., Coradini, A., Drossart, P., Formisano, V., Jaumann, R., Langevin, Y., Matson, D.L., McCord, T.B., Nelson, R.M., Nicholson, P.D., Sicardy, B., Sotin, C., 2006. Composition and physical properties of Enceladus' surface. Science 311, 1425–1428.

Buratti, B.J., Cruikshank, D.P., Brown, R.H., Clark, R.N., Bauer, J.M., Jaumann, R., McCord, T.B., Simonelli, D.P., Hibbitts, C.A., Hansen, G.B., Owen, T.C., Baines, K.H., Bellucci, G., Bibring, J.-P., Capaccioni, F., Cerroni, P., Coradini, A., Drossart, P., Formisano, V., Langevin, Y., Matson, D.L., Mennella, V., Nelson, R.M., Nicholson, D.P., Sicardy, B., Sotin, C., Roush, T.L., Doderlund, K., Muradyan, A., 2005. Cassini Visual and Infrared Mapping Spectrometer observations of Iapetus: Detection of CO_2. Astrophys. J. 622, L149–L152.

Carusi, A., Massaro, E., 1978. Statistics and mapping of asteroid concentrations in the proper elements space. Astron. Astrophys. Suppl. 34, 81–90.

Cerroni, P., Coradini, A., 1995. Multivariate classification of multispectral images: An application to ISM martian spectra. Astron. Astrophys. Suppl. 109, 585–591.

Clark, R.N., Roush, T.L., 1984. Reflectance spectroscopy—Quantitative analysis techniques for remote sensing applications. J. Geophys. Res. 89, 6329–6340.

Clark, R.N., Brown, R.H., Jaumann, R., Cruikshank, D.P., Nelson, R.M., Buratti, B.J., McCord, T.B., Lunine, J., Hoefen, T., Curchin, J.M., Hansen, G., Hibbitts, K., Matz, K.-D., Baines, K.H., Bellucci, G., Bibring, J.-P., Capaccioni, F., Cerroni, P., Coradini, A., Formisano, V., Langevin, Y., Matson, D.L., Mennella, V., Nicholson, P.D., Sicardy, B., Sotin, C., 2005. Compositional maps of Saturn's moon Phoebe from imaging spectroscopy. Nature 435, 66–69.

Coradini, A., Fulchignoni, M., Gavrishin, A.I., 1976. Classification of lunar rocks and glasses by a new statistical technique. Moon 16, 175–190.

Coradini, A., Fulchignoni, M., Fanucci, O., Gavrishin, A.I., 1977. A FORTRAN V program for a new classification technique: The G-mode central method. Comput. Geosci. 3, 85–105.

Coradini, A., Giovannelli, F., Polimene, M.L., 1983. A statistical X-ray QSOs classification. In: International Cosmic Ray Conference Papers, vol. 1. Tata Institute of Fundamental Research, Bombay, pp. 35–38. A85-22801 09-93.

Coradini, A., Cerroni, P., Forni, O., Bibring, J.-P., Gavrishin, A.I., 1991. G-mode classification of martian infrared spectral data from ISM-Phobos 2. Proc. Lunar Sci. Conf. 22, 243.

Cruikshank, D.P., Bell, J.F., Gaffey, M.J., Brown, R.H., Howell, R., Beerman, C., Rognstad, M., 1983. The dark side of Iapetus. Icarus 53, 90–104.

Cruikshank, D.P., Veverka, J., Lebofsky, L.A., 1984. Satellites of Saturn—Optical properties. In: Gehrels, T., Matthews, M.S. (Eds.), Saturn. Univ. of Arizona Press, Tucson, AZ, pp. 640–667.

Cruikshank, D.P., Wegryn, E., Dalle Ore, C.M., Brown, R.H., Baines, K.H., Bibring, J.-P., Buratti, B.J., Clark, R.N., McCord, T.B., Nicholson, P.D., Pendleton, Y.J., Owen, T.C., Filacchione, G., Coradini, A., Cerroni, P., Capaccioni, F., Jaumann, R., Nelson, R.M., Sotin, C., Bellucci, G., Combes, M., Langevin, Y., Sicardy, B., Matson, D.L., Formisano, V., Drossart, P., Mennella, V., 2007. Hydrocarbons on Saturn's satellites Iapetus and Phoebe. Icarus, doi:10.1016/j.icarus.2007.04.036, in press.

Erard, S., Cerroni, P., Coradini, A., 1991. Automatic classification of spectral types in the equatorial regions of Mars. Bull. Am. Astron. Soc. 24, 978. Abstract 24.14-P.

Gavrishin, A.I., Coradini, A., Fulchignoni, M., 1980. Trends in the chemical composition of lunar rocks and glasses. Geokhimiia, 359–370 (in Russian).

Gavrishin, A.I., Coradini, A., Cerroni, P., 1992. Multivariate classification methods in planetary sciences. Earth Moon Planets 59, 141–152.

Giovannelli, F., Coradini, A., Polimene, M.L., Lasota, J.P., 1981. Classification of cosmic sources—A statistical approach. Astron. Astrophys. 95, 138–142.

Hansen, G.B., 2002. A method of measuring surface ice abundance: Application to Ganymede. Lunar Planet. Sci. 33. Abstract 1060.

Jacobson, R.A., Antreasian, P.G., Bordi, J.J., Criddle, K.E., Ionasescu, R., Jones, J.B., Meek, M.C., Owen Jr., W.M., Roth, D.C., Roundhill, I.M., Stauch, J.R., 2004. The orbits of the major saturnian satellites and the gravity field of the saturnian system. Bull. Am. Astron. Soc. 36, 1097. Abstract 15.02.

Johnson, T.V., Lunine, J.I., 2005. Saturn's moon Phoebe as a captured body from the outer Solar System. Nature 435, 69–71.

McCord, T.B., Hansen, G.B., Clark, R.N., Martin, P.D., Hibbitts, C.A., Fanale, F.P., Granahan, J.C., Segura, M., Matson, D.L., Johnson, T.V., Carlson, R.W., Smythe, W.D., Danielson, G.E., 1998. Non-water-ice constituents in the surface material of the icy Galilean satellites from the Galileo near-infrared mapping spectrometer investigation. J. Geophys. Res. 103 (E4), 8603–8626.

McCord, T.B., Coradini, A., Hibbitts, C.A., Capaccioni, F., Hansen, G.B., Filacchione, G., Clark, R.N., Cerroni, P., Brown, R.H., Baines, K.H., Bellucci, G., Bibring, J.-P., Buratti, B.J., Bussoletti, E., Combes, M., Cruikshank, D.P., Drossart, P., Formisano, V., Jaumann, R., Langevin, Y., Matson, D.L., Nelson, R.M., Nicholson, P.D., Sicardy, B., Sotin, C., 2004. Cassini VIMS observations of the Galilean satellites including the VIMS calibration procedure. Icarus 172, 104–126.

Miller, E., Klein, G., Juergens, D., Mehaffey, K., Oseas, J., Garcia, R., Giandomenico, A., Irigoyen, B., Hickock, R., Rosine, D., Sobel, H., Bruce, C., Flamini, E., De Vidi, R., Reininger, F., Dami, M., et al., 1996. The Visual and Infrared Mapping Spectrometer for Cassini. Proc. SPIE 2803, 206–220.

Orosei, R., Bianchi, R., Coradini, A., Espinasse, S., Federico, C., Ferriccioni, A., Gavrishin, A.I., 2003. Self-affine behavior of martian topography at kilometer scale from Mars Orbiter Laser Altimeter data. J. Geophys. Res. 108 (E4), doi:10.1029/2002JE001883.

Owen, T.C., Cruikshank, D.P., Dalle Ore, C.M., Geballe, T.R., Roush, T.L., de Bergh, C., 1999. Detection of water ice on Saturn's satellite Phoebe. Icarus 140, 379–382.

Pollack, J.B., Burns, J.A., Tauber, M.E., 1979. Gas drag in primordial circumplanetary envelopes—A mechanism for satellite capture. Icarus 37, 587–611.

Porco, C.C., Baker, E., Barbara, J., Beurle, K., Brahic, A., Burns, J.A., Charnoz, S., Cooper, N., Dawson, D.D., Del Genio, A.D., Denk, T., Dones, L., Dyudina, U., Evans, M.W., Giese, B., Grazier, K., Helfenstein, P., Ingersoll, A.P., Jacobson, R.A., Johnson, T.V., McEwen, A., Murray, C.D., Neukum, G., Owen, W.M., Perry, J., Roatsch, T., Spitale, J., Squyres, S., Thomas, P.C., Tiscareno, M., Turtle, E., Vasavada, A.R., Veverka, J., Wagner, R., West, R., 2005. Cassini Imaging Science: Initial results on Phoebe and Iapetus. Science 307, 1237–1242.

Soter, S., 1974. Brightness of Iapetus. In: IAU Colloq. 28. Cornell University, August 1974.

Spencer, J.R., Pearl, J.C., Segura, M., 2004. Cassini Composite Infrared Spectrometer (CIRS) observations of Phoebe's thermal emission. In: American Geophysical Union, Fall Meeting 2004. Abstract P43B-03.

Strazzulla, G., Leto, G., Gomis, O., Satorre, M.A., 2003. Implantation of carbon and nitrogen ions in water ice. Icarus 164, 163–169.

Thekaekara, M.P., 1973. In: Drummond, A.J., Thekaekara, M.P. (Eds.), The Extraterrestrial Solar Spectrum. Institute of Environmental Sciences, Mount Prospect, IL, p. 114.

Thomas, P., Veverka, J., Morrison, D., Davies, D., Johnson, T.V., 1983. Saturn's small satellites—Voyager imaging results. J. Geophys. Res. 88, 8736–8742.

Tosi, F., Coradini, A., Gavrishin, A.I., Adriani, A., Capaccioni, F., Cerroni, P., Filacchione, G., Brown, R.H., 2005. G-mode classification of spectroscopic data. Earth Moon Planets 96, 165–197.